Pulsed Operation of a Weakly-Dispersive, Leaky-Wave Antenna

A Causal Numerical Study

Gu, Junhong; Stumpf, Martin; Neto, Andrea; Lager, Ioan E.

Important note
To cite this publication, please use the final published version (if applicable).
Please check the document version above.

Pulsed Operation of a Weakly Dispersive, Leaky Wave Antenna: A Causal Numerical Study

Junhong Gu⬡, *Student Member, IEEE*, Martin Stumpf⬡, *Senior Member, IEEE*, Andrea Neto⬡, *Fellow, IEEE*, and Ioan E. Lager⬡, *Senior Member, IEEE*

Abstract— A strictly causal numerical study of the pulsed operation of a weakly dispersive, leaky wave (LW) antenna is presented. The intricacies at the forefront of the electromagnetic (EM) field radiated from a gap-fed slot in a perfectly electrically conducting (PEC) sheet are evidenced for the first time. The radical effect of a free-space gap separating the PEC sheet from the dielectric half-space into which the slot radiates is demonstrated, thus providing time-domain (TD) arguments for the effectiveness of this essential element of leaky-lens antennas (LLAs). The response of the gapped structure to an excitation consisting of pulse trains is evaluated. The discussed results pave the way toward building a genuine TD counterpart of the LW radiation from gap-fed slots. Furthermore, they are conditional to understanding the transients occurring in between intervals when a steady-state, time-harmonic (TH) operation can be assumed, an extremely relevant ingredient to implementing highly complex modulations in carrier-based, wireless transfer.

Index Terms— Leaky wave (LW) antennas, numerical analysis, time-domain (TD) analysis.

I. INTRODUCTION

THE surging demand for ultrahigh data throughput and low latency that drives the evolutions in wireless communication demands disruptive physical-layer innovations, with terahertz technology being widely seen as pivotal to both present and upcoming (6G) networks [1]. At channel level, the viability of any approach hinges upon the availability of high-performance radiators. In this respect, the planarly fed, leaky-lens antenna (LLA) introduced in [2] established itself as the reference for (sub-)terahertz, nondispersive purposes, with a large selection of implementations of this concept [3], [4], [5], [6], [7], [8] conclusively demonstrating its adequacy. Functionally, LLAs make effective use of the radiation from a gap-fed slot located at a free-space–dielectric interface, this

canonic configuration being extensively examined in [9] and [10]. The decisive achievement of [2] was inserting an air gap between the slot and the dielectric half-space, thus resolutely improving the beam focusing.

It is noted that [2], [9], [10], [11], [12], and [13], much like the majority of the literature on leaky wave (LW) radiation, opted for a frequency-domain (FD) analysis, a choice stemming from the effectiveness of the pertaining analytic instruments. However, this avenue's adequacy becomes problematic in ultrahigh data rate systems: irrespective of code optimization [1], exceptionally high-frequency digital modulation of the carrier is unavoidable, this raising serious concerns about the validity of a steady-state, time-harmonic (TH) assumption. These concerns will be aggravated in multiuser scenarios by the agile beam scanning, an extreme situation being that of the networks of unmanned aerial vehicles (UAVs) discussed in [14].

The alternative is resorting to the time-domain (TD) analysis of the radiators, an avenue presenting the additional benefit of providing clear, justifiable bounds for the applicability of FD strategies. However, such approaches are remarkably scarce in the literature concerning LW radiation, with [15] being one of the isolated exceptions. To remedy this situation, Štumpf et al. [16] examined some configurations associated with LW radiation and established correspondences between typical TH LW features and their TD counterparts. For focusing on conceptual clarifications, that paper explored exclusively electromagnetic (EM) problems that lend themselves to an analytic handling. It then excluded the LLAs specific structures, namely, the gap-fed slot at a free-space–dielectric interface and the one containing an additional free-space gap, since an analytic TD treatment of these two EM problems is not available at this moment.

This article presents, for the first time, a numerical, *rigorously causal, TD analysis* of the LLA-related canonical configuration in [2] and of its precursor [9]. Placing the examined EM problems within a *fully controlled* numerical environment establishes the appropriate framework for revealing the intricacies of the temporal evolution and spatial distributions at the forefront of *any* time-windowed-excited EM field radiated by a slot in the presence of a free-space–dielectric interface. In the process, the validity of the theoretical predictions formulated in [16] and, subsequently, in [17] will be confirmed. At the same time, the experiments will give credible evidence and justification for the influence

of the air gap on the field penetration into the dielectric half-space. To conclude with, the effect of the EM field buildup in the case of a pulse train will be exemplified. Apart from their intrinsic practical applicability, the presented results offer compelling incentives for attempting the construction of TD analytical models of the field behavior at the wave's forefront (a decidedly hard EM problem) and, at the same time, readily supply the needed reference results for the assessment of those models.

This article proceeds by presenting the configurations under study and cataloging a number of features the occurrence of which will be programmatically monitored in the numerical experiments. The next step will be examining these configurations via illustrative TD signatures and field snapshots in relevant cross sections. The field buildup for pulse trains will be evaluated for the air-gapped configuration, only. This article will be rounded off by outlining the practical impact of the study's main findings and by drawing the final conclusions. This article is complemented by an online Supplementary Material [18] comprising a detailed description of the employed pulse shapes, an analysis of the configurational impulse response, and an extended set of simulation results.

II. ANALYSIS METHODOLOGY

A. Investigated Configurations

This study concerns layered structures. Position is specified with respect to a Cartesian reference frame with origin O and three mutually orthogonal unit vectors $\{\boldsymbol{i}_x, \boldsymbol{i}_y, \boldsymbol{i}_z\}$, and the time coordinate is t. Position vectors are denoted as $\boldsymbol{r} = x\boldsymbol{i}_x + y\boldsymbol{i}_y + z\boldsymbol{i}_z$. The EM field is examined via its representative electric field $\boldsymbol{E}(\boldsymbol{r}, t) = E_x(\boldsymbol{r}, t)\boldsymbol{i}_x + E_y(\boldsymbol{r}, t)\boldsymbol{i}_y + E_z(\boldsymbol{r}, t)\boldsymbol{i}_z$ (the compact $E_{x,y,z}$ notation will be henceforth employed). The embedding consists of free space with permittivity ε_0 and permeability μ_0, this entailing a wave speed $c_0 = (\varepsilon_0\mu_0)^{-1/2}$. All configurations contain the following: 1) a perfectly electrically conducting (PEC) sheet of vanishing thickness located in the $z = 0$ plane and 2) a lossless, dielectric semi-infinite domain $\mathcal{D} = \{-\infty < x < \infty, -\infty < y < \infty, z > h\}$, with $h \geqslant 0$, inside which $\varepsilon_1 = \varepsilon_r\varepsilon_0$ (with $\varepsilon_r > 1$ being the relative permittivity). The EM wave speed in the dielectric half-space is $c_1 = (\varepsilon_1\mu_0)^{-1/2} < c_0$. The choice for the dielectric medium being lossless is dictated by the programmatic objective to experimentally verify the analytical results established in [2], [9], and [16] that were derived for lossless media, only. Accounting for the effect of the technologically unavoidable losses is deferred to future research.

The examined configuration is shown in Fig. 1. The EM field is radiated by a slot $\mathcal{S} = \{-w/2 < x < w/2, -\infty < y < \infty, z = 0\}$ cut in the PEC sheet at $z = 0$ and fed by a current-source port $\mathcal{I}$ of vanishing cross section, located at $\{-w/2 < x < w/2, y = 0, z = 0\}$ (the slot's length will be truncated to $2l$ in numerical experiments). The port injects a *causal*, preferably time-windowed, current pulse $i(t)$. The first configuration, henceforth referred to as Configuration A, corresponds to $h = 0$. It will be used for demonstrating the validity of the conclusions of [16] and establishing correspondences with the observations in [9].
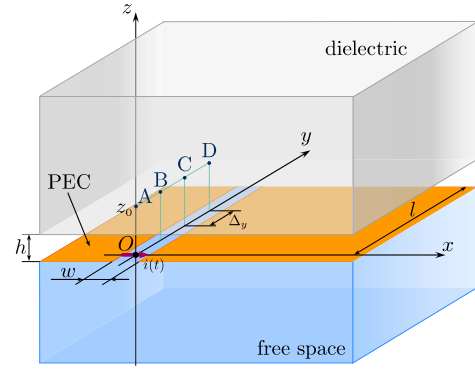

Fig. 1. Two-media configuration comprising two homogeneous and isotropic half-spaces and a PEC sheet of negligible thickness in which a narrow slot is cut. The dielectric half-space is spaced from the PEC sheet by $h = \xi w$, with $0 \leqslant \xi < 2$. The slot is fed by a current-source-type port injecting a *causal* current pulse $i(t)$.

Its analysis will comprise illustrative TD signatures at four equidistant field points A–D, spaced at Δ_y, and field snapshots in the $x = 0$ and $y = 0$ planes. The feature part of the study concerns Configuration B that is obtained by elevating the dielectric half-space at $h > 0$. The gap between the PEC sheet at $z = 0$ and the dielectric half-space $\mathcal{D}$ is filled with free space. The EM field analysis will again consist of representative TD signatures at field points A–D (inasmuch as located inside $\mathcal{D}$) and, primarily, field snapshots in the $x = 0$ and $y = 0$ planes.

Most reported experiments will examine the field behavior in the slot's symmetry plane ($x = 0$), where $E_{y,z}$ vanish. Consequently, only E_x will be henceforth inspected. Clearly, $E_{y,z}$ may become nonzero outside the symmetry plane. However, for maintaining the coherence of the account, their investigation is deliberately deferred to future studies. Furthermore, for compensating the effect of the selected (relatively high) ε_r, the field snapshots will plot the normalized $\varepsilon_r E_x$ quantity.

The nature of the weak dispersion properties of the examined slotted structures depends on the value of h. For $h \downarrow 0$ (Configuration A), the propagation constant of the dominant LW is almost constant as a function of frequency, while the attenuation constant increases with frequency. Meanwhile, for h significant in terms of the wavelength (as in Configuration B), the propagation constant equals the average of that in the upper and lower media for low frequencies and decreases to the value in the less dense medium for higher frequencies. As for the attenuation constant, it reflects the effective distance between the slot and the denser medium, with lower attenuation (radiation) for larger distances.

B. EM Features in the Investigated Configurations

The present exploration will focus on singling out specific EM field features that are associated with the (guided) propagation along a plane free-space–dielectric interface. In this respect, Štumpf et al. [16] cataloged, for the gap-excited slot in Configuration A, three types of waves occurring *inside* the dielectric half-space ($z > 0$).
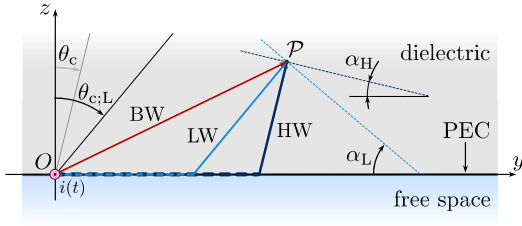
Fig. 2. Explicative for the angles corresponding to the waves occurring *inside* the dielectric half-space (cross section in the $x = 0$ plane). The three types of waves (HW, LW, and BW) that arrive at a point $\mathcal{P}$ beyond $\theta_{c;L}$ are shown. Their respective arrival times are $\tau_{a;B} > \tau_{a;L} > \tau_{a;H}$. The shown angles are represented at scale for the case of $\varepsilon_r = 16$, as used in this article.

1) Body Waves (BWs)[1]: Such waves exist always. Their wave speed is c_1, and the arrival time of a wave excited by $\mathcal{I}$ and sensed at $(0, y, z)$ is

$$\tau_{a;B} = \left(y^2 + z^2\right)^{1/2}/c_1. \tag{1}$$

2) Head Waves: Such waves only arise outside a cone given by the critical angle θ_c defined by (see Fig. 2)

$$\sin(\theta_c) = c_1/c_0 = 1/\sqrt{\varepsilon_r} \tag{2}$$

amounting for points of coordinates $(0, y, z)$ to the condition

$$|y|/\left(y^2 + z^2\right)^{1/2} > \sin(\theta_c). \tag{3}$$

In [17], it was shown that HWs excited by $\mathcal{I}$ and sensed at $(0, y, z)$ propagate along a path that minimizes the propagation time, the entailed arrival time being

$$\begin{aligned}
\tau_{a;H} &= |y|/c_0 + z\left(c_1^{-2} - c_0^{-2}\right)^{1/2} \\
&= \left(|y| + z\sqrt{\varepsilon_r - 1}\right)/c_0.
\end{aligned} \tag{4}$$

That paper also showed that the HW wavefront is tilted with respect to the plane interface at an angle (see Fig. 2)

$$\alpha_H = \arctan\left(1/\sqrt{\varepsilon_r - 1}\right) = \theta_c. \tag{5}$$

3) Leaky Waves: Štumpf et al. [16] evidenced a field extremum appearing at points where HWs are intercepted, its occurrence being between the arrival of the relevant HW and BW. This extremum shares certain commonalities with phenomena associated with FD LW-type radiation, most importantly the same decay with respect to the distance to the interface. The complex physics leading to this enhancement was discussed in detail in [17, Sec. III.B]. A characteristic feature of these LWs is their arrival time at $(0, y, z)$, with $z > 0$

$$\begin{aligned}
\tau_{a;L} &= \frac{|y|}{c_0}\left(\frac{c_0^2/c_1^2 + 1}{2}\right)^{1/2} + \frac{z}{c_0}\left(\frac{c_0^2/c_1^2 - 1}{2}\right)^{1/2} \\
&= \frac{|y|}{c_0}\left(\frac{\varepsilon_r + 1}{2}\right)^{1/2} + \frac{z}{c_0}\left(\frac{\varepsilon_r - 1}{2}\right)^{1/2}.
\end{aligned} \tag{6}$$

[1]BWs are commonly referred to in FD publications as *space waves* [10], [19], [20]. Following a terminology established in [21, Ch. 2], head waves (HWs) are designated in the FD literature as *lateral waves* (see also the discussion on the terminology in [22] and the definitions in [10]).

As shown in [16], LWs are also associated with a critical angle $\theta_{c;L}$ defined by (see Fig. 2)

$$\sin(\theta_{c;L}) = \left(\frac{1 + c_1^2/c_0^2}{2}\right)^{1/2} = \left(\frac{\varepsilon_r + 1}{2\varepsilon_r}\right)^{1/2} \tag{7}$$

which is identical to the LW cone's limit given in [10]. Their wavefront tilting with respect to the interface can be derived by repeating the reasoning in [17] for a propagation speed along the interface

$$c_L = c_0\left(\frac{2}{c_0^2/c_1^2 + 1}\right)^{1/2} = c_0\left(\frac{2}{\varepsilon_r + 1}\right)^{1/2} \tag{8}$$

the value of the relevant (acute) angle being (see Fig. 2)

$$\alpha_L = \arctan\left(\sqrt{\frac{\varepsilon_r + 1}{\varepsilon_r - 1}}\right) = \theta_{c;L}. \tag{9}$$

It must be stressed that expressions (6)–(9) were derived in [16] for a very narrow, weekly dispersive slot.

This study will endeavor to identify the manifestation of the arrival times $\tau_{a;B}$, $\tau_{a;H}$, and $\tau_{a;L}$ in TD field signatures, and the wavefront angles α_H and α_L in field snapshots.

4) Phenomenological Discussion of the Wave Types: The phenomenological interpretation of the three types of waves was dealt with in [17, Sec. III.B]. The main elements therein are reiterated by examining the waves radiated by the current-source port $\mathcal{I}$ and received at an arbitrary observation point $\mathcal{P}$ beyond $\theta_{c;L}$ (see Fig. 2). The first wave arriving at $\mathcal{P}$ is the HW, its path minimizing the travel time by having the longest possible fast propagation along the interface, followed by the shortest path through the dielectric. Its corresponding wavefront is tilted with respect to the air–dielectric interface at $\alpha_H = \theta_c$. The second wave arriving at $\mathcal{P}$ is the LW, that has a (substantially) shorter fast travel along the interface and a longer slow travel through the dielectric. Its corresponding wavefront is tilted at $\alpha_L = \theta_{c;L}$, this giving supplementary support to the fact that the LWs evidenced in [16] are only possible beyond a critical angle. The last wave to arrive is the BW, which travels along a straight path situated exclusively inside the dielectric.

C. Computational Choices

All numerical experiments were performed by means of the finite-integration technique (FIT) as implemented in CST Microwave Suite®. A relatively large relative permittivity, namely, $\varepsilon_r = 16$, entailing a wave speed in dielectric $c_1 = c_0/4$, was intentionally adopted for allowing a clear distinction between HWs and the trailing BWs (the chosen value is comparable with the relative permittivity of silicon $\varepsilon_{r,Si} = 11.9$). For the chosen ε_r, the critical angles are $\theta_c = 17.6°$ and $\theta_{c;L} = 47.6°$, respectively. With reference to Fig. 1, $w = 1\,\mathrm{mm}$, and field points A–D were at $z_0 = 1\,\mathrm{mm}$ and $\Delta_y = 4\,\mathrm{mm}$. The feeding current-source port $\mathcal{I}$ was placed at the center of the chosen domain of computation. For both configurations $|x| \leqslant 20\,(\mathrm{mm})$ and $|y| \leqslant 25\,(\mathrm{mm})$ ($l = 25\,\mathrm{mm}$), the dielectric slab had a height of 5 mm, and the free-space region under the PEC was 5-mm high. The

domain's extension in the positive z-direction depended on h, varying between 15 mm (Configuration A) and 16.5 mm (Configuration B, for maximum h). The parallelepipedic domains of computation were discretized via nonuniform hexahedral meshes designed to ensure eight cells in the slot, the highest mesh density accommodated by the resources of the employed computer. To this end, the software's automatic mesh generator was set to a (conventional) maximum reference frequency $f_{max} = 40$ GHz, in conjunction with a 15 cells/λ minimum step, the resulting meshes comprising between 6 860 532 cells (Configuration A) and 7 507 752 cells (Configuration B, for maximum h). All boundary conditions were of the perfectly matched layer (PML) type. However, correlating the domain sizes with the employed time-windowed excitation (see [23]) largely precluded boundary reflections from reaching the area of interest within the examined time window.

As indicated above, the port $\mathcal{I}$ injects a time-windowed current pulse $i(t)$. Two *unipolar* shapes were considered, namely, the triangular $\Delta(t)$ and the windowed-power WP(t) ones (see [18, Sec. II] for details). The former shape was only used for testing the deconvolution of the FIT-calculated signatures at field points A–D in Fig. 1, as explained in [18, Sec. III]. Owing to the similarity of the signatures obtained by feeding with either $\Delta(t)$ or WP(t), combined with the superior smoothness of the latter, all numerical experiments reported in this article employ a WP excitation with raising power $\nu = 6$.

Simulations were run on an Intel Core i5-9600KF at 3.7-GHz system with 9-GB RAM, and analyzing each configuration required approximately 10 min, the time for generating the output files excluded. The FIT data were subsequently graphically processed in MATLAB®. As concerns the TD signatures at the field points, it was observed that the FIT-calculated data were affected by extraneous high-frequency oscillations that were attributed to local resonance inside mesh cells. These oscillations were smoothed out via a strategy making use of a moving average over five consecutive points—in some cases, this strategy was applied twice. The smoothed signatures were then aligned by taking the arrival of the HW as a reference, except at point A where the BW was used instead (no HW occur at A). All field snapshots were generated via custom-built, color-coded, plotting functions. Additional elements were superposed in the plots for highlighting some important field features (such as the wavefront tilting). To conclude with, the response to pulse trains was obtained by superposing successive snapshots taken at equally spaced time samples.

III. CONFIGURATION-A STUDY

Configuration A replicates the one discussed in [9], its analysis focusing on the field evolution near the slot. First, TD signatures at field points A–D in Fig. 1 will be extracted from the FIT solution—as demonstrated in [18, Sect. II], these signatures are an excellent approximation of the structure's impulse response. This exercise aims at validating some predictions formulated in [16] for a resembling, but not identical situation, the focus being on identifying features associated with the arrival times in (1), (4), and (6). The next step will be

preparing field snapshots in the $x = 0$ plane, in the proximity of the slot. A special attention will be given to observing the tilting of the wavefront and comparing it with the prediction in (3). Finally, the field distribution in planes orthogonal to the slot will be briefly examined.

A. Representative TD Signatures

The twice smoothed FIT signatures at A–D are shown in Fig. 3. As documented in [18, Table I], these signatures concur extremely well with those corresponding to a $\Delta(t)$ excitation, which, in turn, allows concluding that the WP(t)-excited, FIT signatures are adequate approximations of the configurational impulse response, as well. This observation justifies the choice to effectuate all simulations with a WP(t) excitation (see Section II-C).

For identifying possible features associated with the arrival times in (1), (4), and (6), the relevant instants were marked in Fig. 3. The following observations can be made: 1) the signature at A contains BWs, only and is used for calibration purposes; 2) examining the behavior at B–D evidences the steady elongation of the first lower lobe when moving away from the source, as a result of the increasingly long interval between $\tau_{a;H}$ and $\tau_{a;B}$; at the same time, the lowermost point on the signatures moves increasingly closer to the $\tau_{a;L}$ marker; and 3) there is little evidence of an event around $\tau_{a;B}$, with the BW constituent being engulfed in other contributions. In view of the similarity between the $\Delta(t)$ and WP(t) excited EM fields, these observations coincide with those made in [17].

B. Field Distribution Analysis

The EM field distribution was first examined by means of field snapshots along the slot. The investigation had a twofold focus: 1) the field behavior at the perturbation's forefront, this providing details on the space–time evolution of the HWs and 2) the interval between the arrival of the HWs and that of BWs, where signatures of the LW phenomenon were expected to be recognized. The TD traces in Fig. 3 also offered handles for interpreting the information contained in the snapshots. In addition, the field confinement in the slot region was assessed via orthogonal snapshots.

The space–time propagation in the configuration's symmetry plane $x = 0$ is shown in Fig. 4, the snapshot instants being selected such that to highlight the HWs arrival at B–D. The critical angles θ_c and $\theta_{c;L}$, and the wavefronts at the relevant instants are given in the plots as reference. The plots illustrate the clear disjunction between the "HW zone," namely, the blue region at the front, and the trailing "BW zone," in which the cylindrical wave pattern is evident. A hallmark of these plots is the remarkable agreement between the predicted LW wavefront and the field maxima in the "HW zone" (corresponding to the darkest shades of blue in the relevant region). The slight standing wave pattern forming behind the first BWs in Fig. 4(b) and (c) was attributed to interferences caused by the late ringing along the slot. The snapshot at 80 ps also allows recognizing the TD signature in Fig. 3(b), with the characteristic damped oscillations that are expected in view of the $\delta(t)$-like excitation. To conclude with, the field
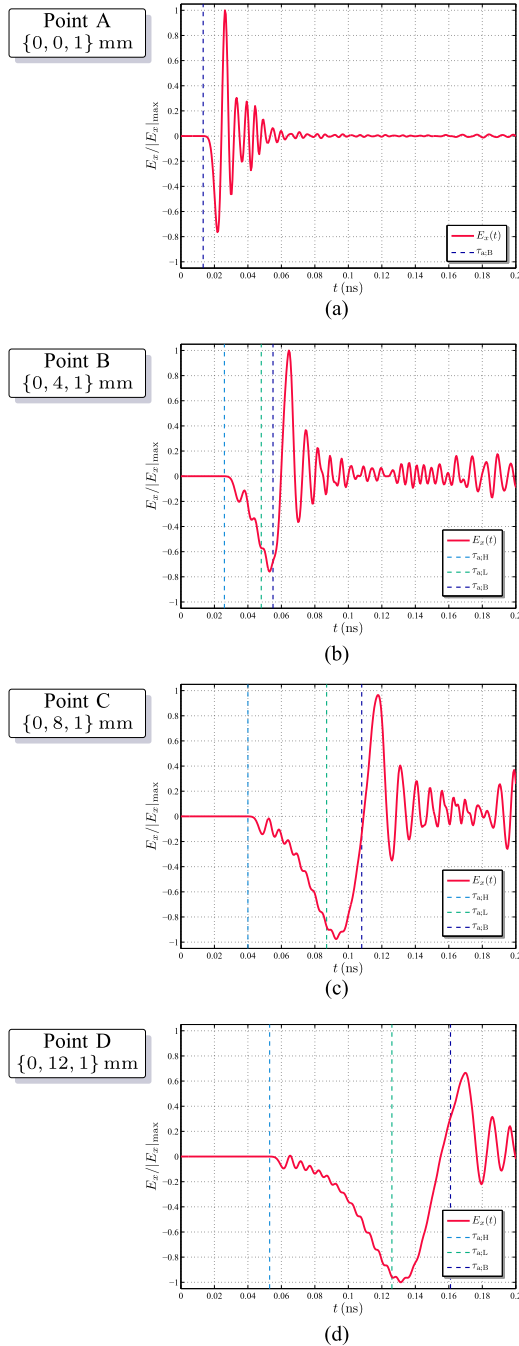
Fig. 3. Responses at the points A–D in Fig. 1 for a WP(t) excitation and a gap height $h = 0.5$ mm: (a) response at point A, (b) response at point B, (c) response at point C, and (d) response at point D. The dashed lines correspond to the arrival times of the relevant wave constituents.

Fig. 4. Field distribution in the $x = 0$ plane at three instants: (a) $t = 40$ ps, (b) $t = 80$ ps, and (c) $t = 110$ ps. $|\varepsilon_r E_x|_{\text{max}}$ is the maximum of $|\varepsilon_r E_x|$ over all snapshots. Points A–D in Fig. 1 are given for reference.

of the HWs in [17], with the field in the dielectric being "pulled" by the fast wave in the free-space underneath. As a result, the wavefront in the dielectric becomes an almost straight line inclined at the slope predicted in (5), the simulated wavefront (as inferred by highlighting the limit of the lowest represented value) practically overlapping the predicted one. Furthermore, $\tau_{a;H}$ at C, as indicated in Fig. 3(c), is perfectly replicated in the simulation. To conclude with, after the HW arrival, the different wave speeds in the two media induce discrepancies along the interface, the field "turbulence" being evident in the snapshot. This type of field propagation cannot but reflect in the wave impedance that, in turn, will influence the radiation properties of the structure, as a whole. The second zoomed-in view focuses on the transition region from the LWs to BWs propagation [see Fig. 5(b)]. The critical angles, the wavefront, and the BW wavefront at 40 ps are given as reference. The plot clearly illustrates two important features: first, there is a manifest field enhancement[2] along the boundary at $\theta_{c;L}$, this being construed as an evidence of the maximum anticipated in [16]. Note also that an alignment

propagation in the slot is also visibly reproduced—here, one must bear in mind that BWs propagate above the interface at $c_1 = c_0/4$, whereas the waves propagate under the interface at c_0, the sharp discrepancy necessarily yielding strong surface currents whose effect reflects in the damped-oscillating field distribution in the vicinity of the slot, its cyclicity following closely that of the BWs.

The snapshot at $t = 40$ ps is detailed in Fig. 5. First, the field behavior at the wave's forefront is shown in Fig. 5(a). The image cogently validates the phenomenological interpretation
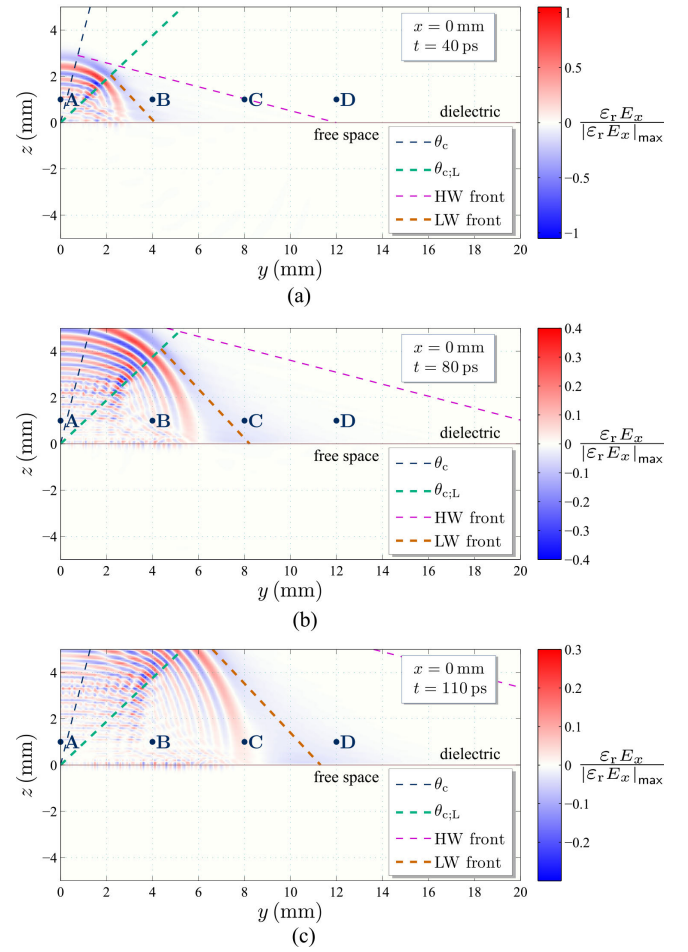
---

[2]Here, and in subsequent analyses, the "field enhancement" is considered with respect to the field values in the examined plane, in the region where the BW radiation is predominant.
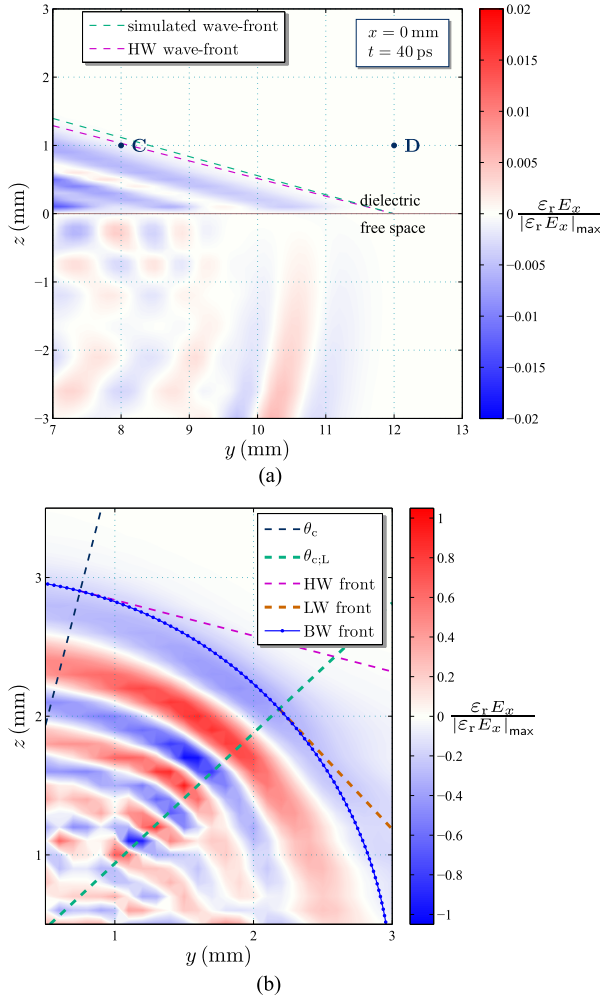
(a)

(b)

Fig. 5. Zoomed-in view on the field distribution in the $y = 0$ plane at $t = 40$ ps [see Fig. 4(a)]. (a) Wave's forefront; points C and D in Fig. 1 are given for reference; the exact and simulated wavefronts are also shown. (b) Transition region from the LWs to BWs propagation; the exact HW and LW wavefronts, and the BW front at 40 ps are also shown. $|\varepsilon_r E_x|_{\mathsf{max}}$ is the maximum of $|\varepsilon_r E_x|$ over all snapshots in Fig. 4.

of the maxima locations can be recognized in the plot, this alignment being associated with a wavefront. This wavefront is (almost) orthogonal to the $\theta_{c;L}$ line, which, again, concurs with the prediction in (5). Second, the cylindrical pattern clearly bends and becomes increasingly blurred in the region beyond $\theta_{c;L}$ as a result of the complex interaction between various delayed HWs and the BWs. This induces a modulation of the propagating BWs whose effect is comparable with that examined in [9] and [10].

The last study concerned the field distribution in the $y = 0$ plane (see Fig. 6). Since $E_x = 0$ along the PEC sheet, this structure only supports BWs in the E_x propagation, their characteristic signature being obvious in Fig. 6(c). In the dielectric, E_x propagates upward, but vanishes rapidly in sideway directions. Furthermore, the wave propagating in the free-space underneath induces currents in the PEC, this being evidenced by the field pattern *immediately under* the sheet.

IV. CONFIGURATION-B STUDY

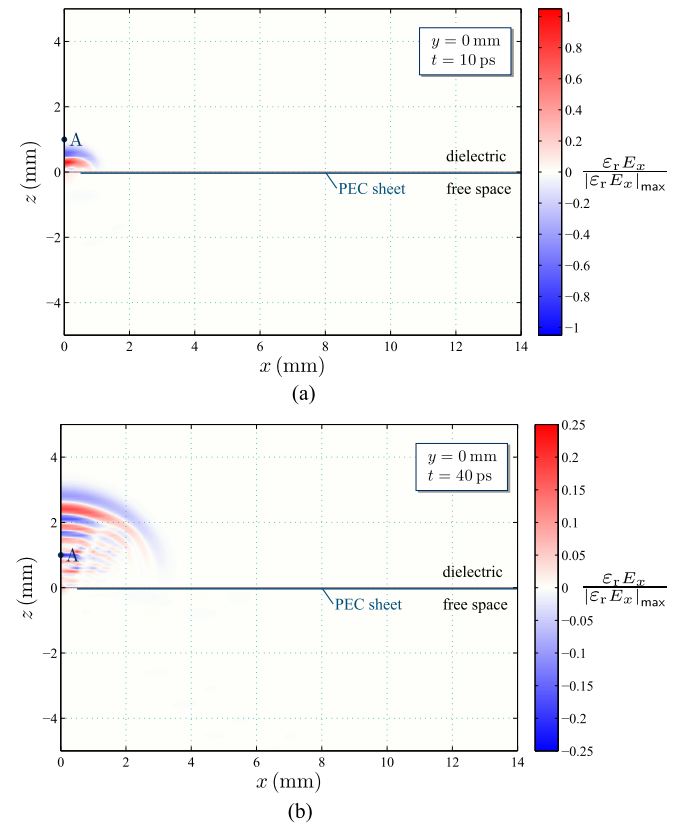The limitations of Configuration A when used for feeding lens antennas were solved in [2] by adding a free-space (air)

(a)

(b)

Fig. 6. Field distribution in the $y = 0$ plane at two instants: (a) $t = 10$ ps and (b) $t = 40$ ps. $|\varepsilon_r E_x|_{\mathsf{max}}$ is the maximum of $|\varepsilon_r E_x|$ over all snapshots. Point A in Fig. 1 is given for reference.

gap above the slotted PEC sheet. This approach relied on the existence of a "shadow boundary" marking the transition from the space waves (BWs in TD terminology, see [16, Appendix]) radiation to the LW-type one. A pronounced field enhancement manifests itself along the boundary, the angle γ_{sb} at which it occurs (see [10, Table II]) depending on the wave speed *underneath* the interface. By introducing the air gap, the wave speed increases from c_L in (8) to, practically, c_0, this resulting in the boundary coming nearer to the normal and, thus, to an improved illumination of the dielectric lens.

While the analysis in [10] and the innovations inferred in [2] relied entirely on FD arguments, the underlying phenomena should have a TD counterpart. In this respect, elevating the dielectric half-space at h (see Fig. 1) allows the waves guided in the slot to travel at c_0. Furthermore, the exciting current source is shifted away from the interface, and the field in the dielectric is produced exclusively by secondary sources induced at the interface by the waves propagating along the slot. As a result, this field consists of a superposition of HWs and BWs created by the moving secondary sources, this mechanism being expected to produce a much more extended "HW zone" at the forefront of the pulsed field.

Configuration B replicates the one at the core of [2], and its examination aims at elucidating the impact of the gap on the radiation properties. The analysis will start by repeating some of the previous experiments, will then proceed to performing
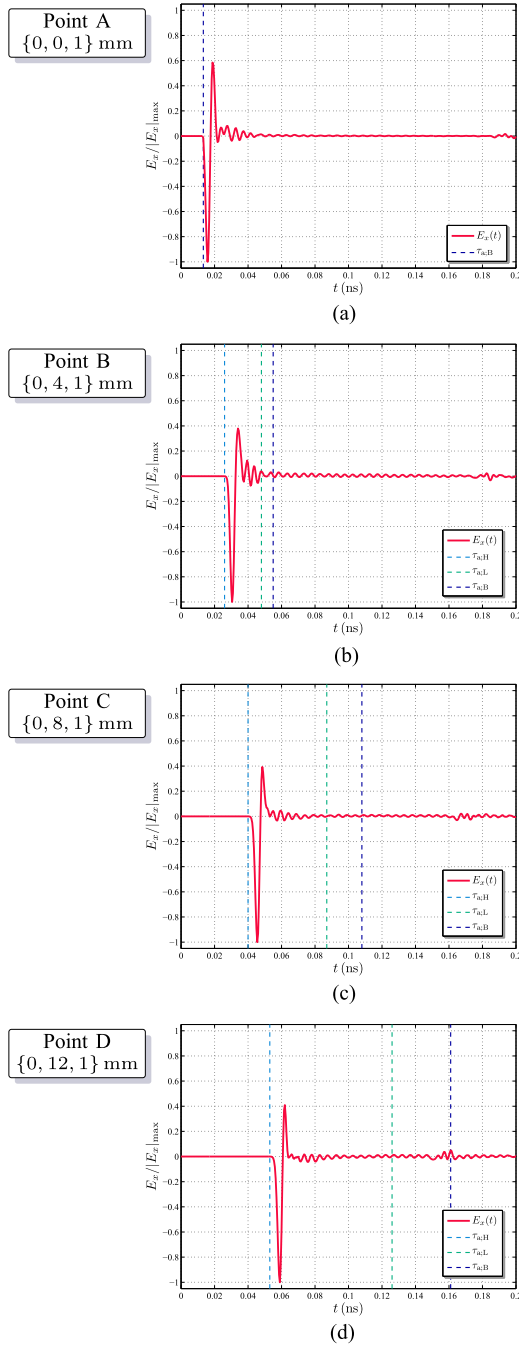
Fig. 7. Responses at the points A–D in Fig. 1 for a WP(t) excitation: (a) response at point A, (b) response at point B, (c) response at point C, and (d) response at point D. The dashed lines correspond to the arrival times of the relevant wave constituents, as shown in Fig. 3.

a parametric study of the gap height, and will be concluded by an investigation of the field radiated by pulse trains.

A. Representative TD Signatures

The gap height in Fig. 1 is first set to $h = 0.5\,\text{mm} = w/2$. The TD signatures evaluated at A–D are shown in Fig. 7—the time references in Fig. 3 are marked for facilitating comparisons. Similar to Section III-A, the FIT signatures were twice smoothed via the moving average procedure. The resulting signatures are entirely different from those in Fig. 3, the traces at A–D being, in this case, remarkably similar. This likeness
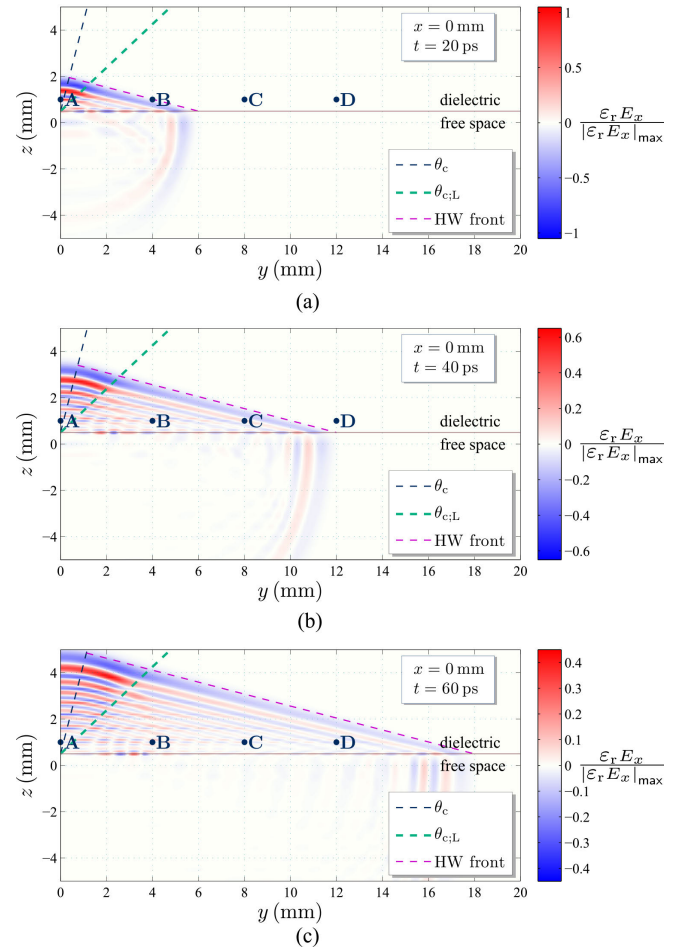

Fig. 8. Field distribution in the $x = 0$ plane, for $h = 0.5\,\text{mm}$, at three instants: (a) $t = 20\,\text{ps}$, (b) $t = 40\,\text{ps}$, and (c) $t = 60\,\text{ps}$. $|\varepsilon_r E_x|_{\text{max}}$ is the maximum of $|\varepsilon_r E_x|$ over all snapshots. Points A–D in Fig. 1 are given for reference.

is in line with the radiation mechanism described above, with the field propagating unrestrained along the slot and producing secondary sources at the interface that, in turn, launch the field inside the dielectric. This complex interaction intermingles HW–BW-type radiations, making their identification hard, if at all possible. The time scale in Fig. 7 was kept the same as in Fig. 3 for underlining that the pulse response is now extremely narrow (its significant part is mostly confined to the excitation's pulsewidth—see [18, Sec. II]).

B. Field Distribution Analysis

To further validate the radiation mechanism, the field is now examined via longitudinal snapshots in the $x = 0$ plane (see Fig. 8). The critical angles θ_c and $\theta_{c;L}$, and the wavefront at the relevant instants are again marked in the plots for reference. Apart from the overall similarity, which was not the case in Fig. 4, these new plots illustrate a quite regular propagation in the free-space region, at least at the wave's forefront. Even more noteworthy, the field propagation in the dielectric is extremely regular, with an almost laminar,[3] extended front

---

[3]The term "laminar" is used here in the sense of the spatial distribution of the field having a layered aspect, with the amplitude curves appearing as almost straight lines.
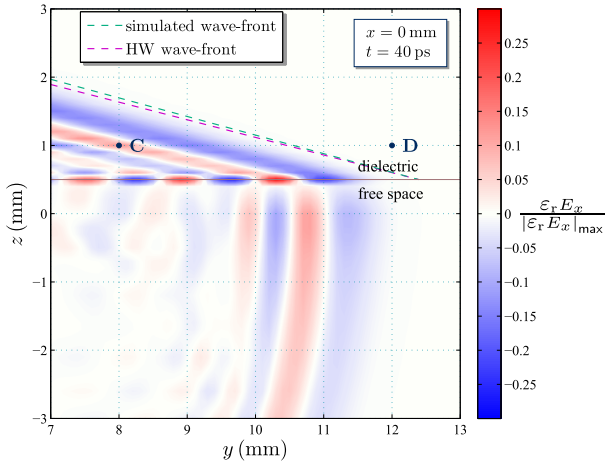
Fig. 9. Zoomed-in view on the field distribution in the $x = 0$ plane at $t = 40$ ps. Points C and D in Fig. 1 are given for reference. The exact and simulated wavefronts are also shown. $|\varepsilon_r E_x|_{\text{max}}$ is the maximum of $|\varepsilon_r E_x|$ over all snapshots in Fig. 8.

region, followed by a wave pattern that is typical for the BWs propagation, an arrangement that is reminiscent of the characteristic juxtaposition of "space waves" and "LWs" in FD analyses [2], [20]. It is also important to observe the abrupt laminar-to-BWs transition (roughly, along $\theta_{c;L}$), while the HWs-to-BWs transition was gradual in Fig. 4—this transition will be examined in more detail in Section IV-D. It should be observed that the simulated wavefront in the pre-BWs region starts extending beyond the HW theoretical front, this being most visible in Fig. 8(c). This effect is interpreted as a computational artifact, as explained in Section V.

A zoomed-in view of the wave's forefront at $t = 40$ ps is shown in Fig. 9. As already observed, the wavefront tilting predicted by (5) is less accurately replicated than in Fig. 5(a). Nonetheless, this deviation remains limited, and one must recall that α_H was calculated for a purely HWs propagation, whereas the field is now a complex combination of (retarded) BWs and HWs! Furthermore, the zoomed-in view manifestly illustrates the "pulling" of the wave in the dielectric, with well-outlined first waves in free space, followed by increasingly disturbed ones, due to the different wave speeds one side and the other of the interface.

As elaborated upon in Section V, the FIT snapshots's timing induces incongruence between the simulated and theoretically predicted HW wavefronts, when the latter is placed according to the wave's travel over the indicated time (in this case, 40 ps). For facilitating comparisons, the HW wavefront was translated in Fig. 9 in the y-direction such that its intersection with the free-space–dielectric interface to coincide with that of the simulated one.

The last step consists of examining the field distribution in the $y = 0$ plane (see Fig. 10). At variance with the behavior exemplified in Fig. 6, the free-space gap allows now the field to propagate sideways, this yielding a dielectric field distribution inside the dielectric that resembles the one along the slot. Another interesting element captured in Fig. 10(b) is the characteristic-guided wave pattern of the free-space propagation in between the PEC sheet and the dielectric.
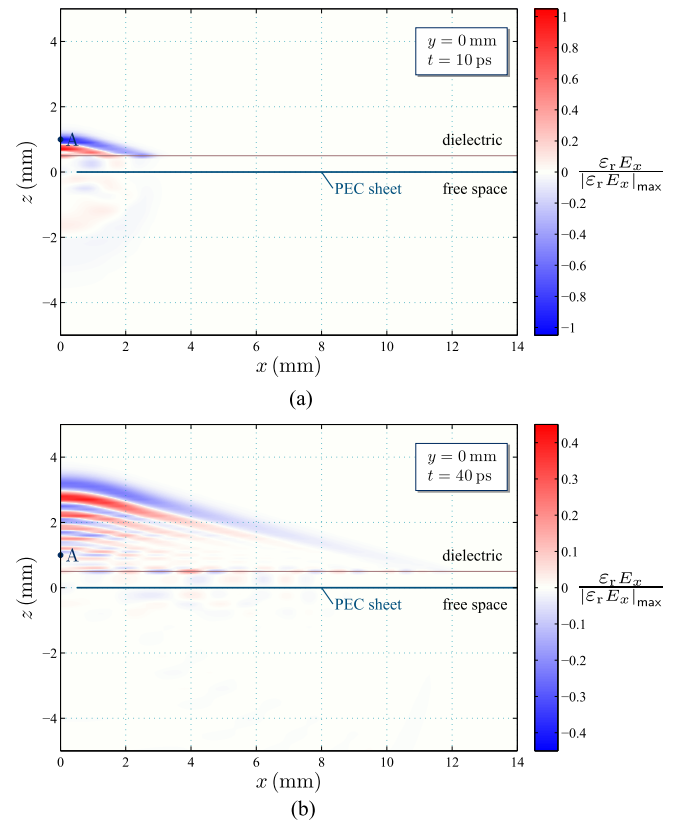

(a)

(b)

Fig. 10. Field distribution in the $y = 0$ plane, for $h = 0.5$ mm, at two instants: (a) $t = 10$ ps and (b) $t = 40$ ps. $|\varepsilon_r E_x|_{\text{max}}$ is the maximum of $|\varepsilon_r E_x|$ over all snapshots. Point A in Fig. 1 is given for reference.

C. Air-Gap Analysis

For assessing the effect of the gap height on the radiation from the slotted PEC sheet, the experiments in Section IV-B were repeated for $h = 1$ mm $= w$ and $h = 1.5$ mm $= 1.5w$. The corresponding longitudinal field distributions are shown in Figs. 11 and 12, respectively. Comparing these plots with those in Fig. 8 evidences similar patterns. However, the contour plots shades indicate increasingly similar peak values of the normalized $\varepsilon_r E_x$ above and below the interface as h increases. Since the field strength under the interface is largely unchanged, the peak values leveling convincingly prove the decrease in field penetration as h increases, a trend already documented by FD analyses [2, Sec. III]. As in Fig. 9, the simulated wavefront deviates from the theoretically predicted α_H. Although the deviation remains small, the angle between the z-axis and the normal to the simulated wavefront diminishes as h increases.

Performing this analysis in the transverse direction, in the $y = 0$ plane (see Figs. 13 and 14) yields alike observations. By comparing Fig. 10 with these figures, it is also noted that the propagation becomes increasingly turbulent as h increases (from an FD perspective, this corresponds to a multimodal propagation, but, evidently, a modal distinction based on cutoff does not apply to a TD analysis [24]). In any event, such a propagation will quite likely affect the radiation efficiency in the configuration and should be avoided.

A fine analysis of the h dependency will plausibly yield an optimum height, but it is clear that $h = 1.5w$ is already too
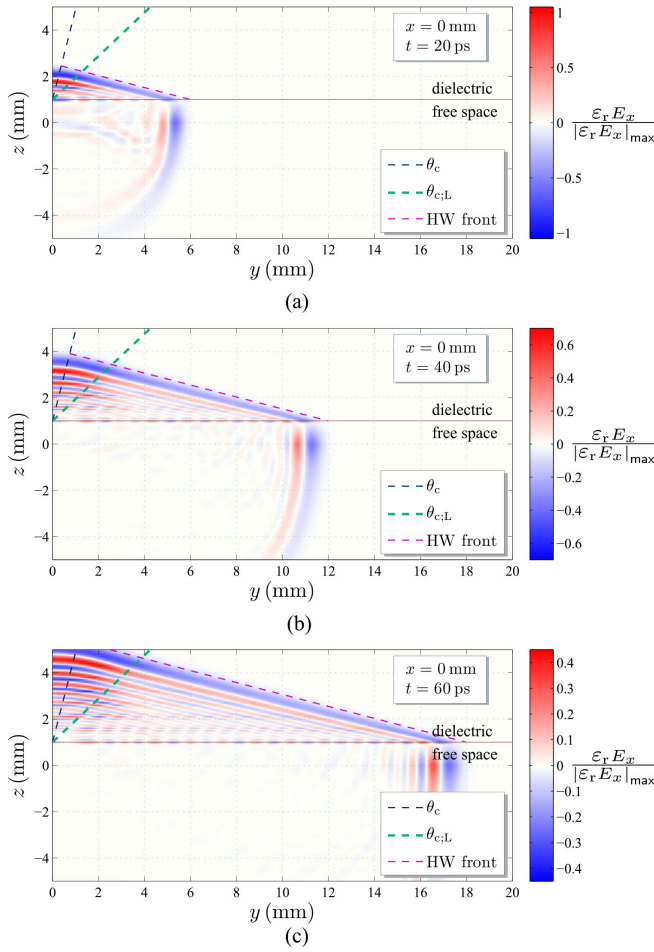
Fig. 11. Field distribution in the $x = 0$ plane, for $h = 1$ mm, at three instants: (a) $t = 20$ ps, (b) $t = 40$ ps, and (c) $t = 60$ ps. $|\varepsilon_r E_x|_{\max}$ is the maximum of $|\varepsilon_r E_x|$ over all snapshots.
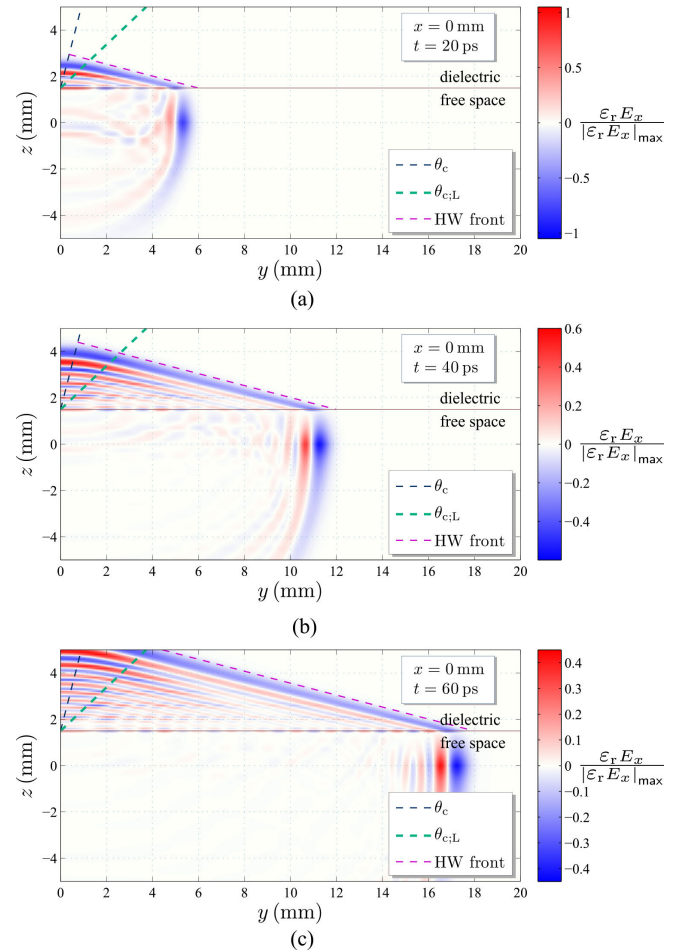

Fig. 12. Field distribution in the $x = 0$ plane, for $h = 1.5$ mm, at three instants: (a) $t = 20$ ps, (b) $t = 40$ ps, and (c) $t = 60$ ps. $|\varepsilon_r E_x|_{\max}$ is the maximum of $|\varepsilon_r E_x|$ over all snapshots.

large for being technically interesting. Consequently, this gap height will be skipped in the subsequent tests.

D. Field Buildup for Pulse Trains

All previous tests were carried out for single-pulse excitations. While such an exercise is extremely relevant from a conceptual point of view, the corresponding energy of the signal will undeniably be very low. Consequently, pulse trains are usually employed in practical applications for ensuring the signal's detectability. By gradually increasing the length of these trains, the system will progress toward a steady-state, periodic operation, thus providing grounds for comparisons with standard, steady-state, TH results.

The field excited by pulse trains is examined by superposing pulse responses at equally spaced instants, this corresponding to an ideal, nonringing, periodic pulse feeding. The longitudinal field distribution obtained by combining four pulsed responses is shown in Fig. 15 for $h = 0.5$ mm and $h = 1$ mm (the critical angles θ_c and $\theta_{c;L}$ are given for reference). Note that, for the chosen domain of computation, extending the analysis beyond 80 ps will result in boundary reflections that will alter the field in the region of interest, and thus, this study is confined to superposing at most four pulse responses.

The plots show, for the chosen pulse repetition rate, a regular wave propagating into the dielectric (in 3-D, this corresponds to a conical wave). A highly relevant feature is the clear-cut division of the field distribution into circular, BWs-type, and laminar-type zones, with an abrupt transition in between. The pulse-train analysis allowed delineating the limit of the laminar propagation (the "LW simulated" lines in Fig. 15), that corresponds remarkably well with the $\theta_{c;L}$ line! Corroborating these observations and accounting for the conclusions drawn in Section III allow conjecturing that this pre-BWs zone is, in fact, *a region of LW-type radiation*.

Examining the superposition of more responses also allowed inferring an alignment of field enhancement (the "enhancement" lines in Fig. 15). While in the gapless case the enhancement manifested itself along the $\theta_{c;L}$ line [see Fig. 5(b)], the maxima alignments now move closer to the z-axis, the relevant angles being 33.7° and 29.9° for $h = 0.5$ mm and $h = 1$ mm, respectively. This evolution is in striking accordance with the "shadow boundary" analysis in [2] and confirms the validity of using pulse-train studies as a buildup toward constructing the link between the single-pulse, TD investigation and traditional, FD studies. To conclude with, the contour plot shades reflect a noticeable diminishing of the field radiated into the dielectric in Fig. 15(b); this
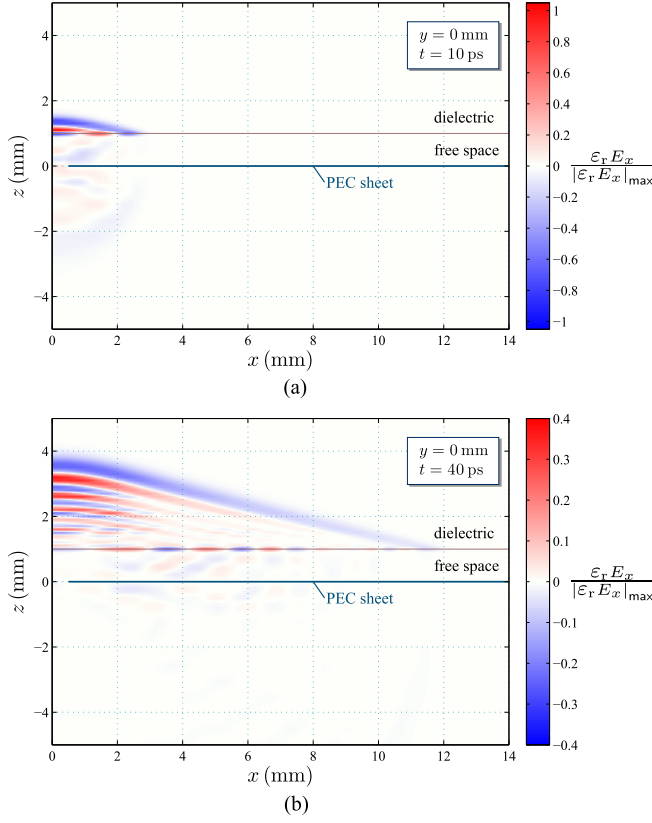
Fig. 13.   Field distribution in the $y = 0$ plane, for $h = 1$ mm, at two instants: (a) $t = 10$ ps and (b) $t = 40$ ps. $|\varepsilon_\mathrm{r} E_x|_{\max}$ is the maximum of $|\varepsilon_\mathrm{r} E_x|$ over all snapshots.

Fig. 14.   Field distribution in the $y = 0$ plane, for $h = 1.5$ mm, at two instants: (a) $t = 10$ ps and (b) $t = 40$ ps. $|\varepsilon_\mathrm{r} E_x|_{\max}$ is the maximum of $|\varepsilon_\mathrm{r} E_x|$ over all snapshots.

suggesting that the optimum gap height is, probably, close to $h = w/2$.

An interesting attribute in the FD description of LW is the field's "improper" character (its exponential increase away from the interface, up until the "shadow boundary"). Capturing the field's "improper" character via TD, causal study is an intriguing topic of future research, and field buildup experiments as those reported in Fig. 15 may give clues on the physical mechanism behind this unusual behavior.

Similar numerical experiments were conducted for the transverse propagation in the $y = 0$ plane. The aggregation of four pulse responses is illustrated in Fig. 16, with the pulse repetition being deliberately halved for examining possible frequency-induced effects. The critical angles θ_c and $\theta_{\mathrm{c;L}}$ are again given for reference. These graphs illustrate a similar division of the field distribution into circular, BWs-type, and laminar-type zones. The limits of the laminar propagation regions were marked as "LW simulated," those lines being again close to $\theta_{\mathrm{c;L}}$, although they tend to lean away from the z-axis as h increases. No frequency-induced effects were noticed. Corroborating the information in Fig. 16 with that following from Fig. 15 conclusively shows that the BWs-type propagation will be confined to an elliptical region and, thus, will be highly propitious for illuminating a lens.

V. PRACTICAL IMPACT OF THE SIMULATION RESULTS

As stated in Section I, LW antennas are currently studied and designed exclusively in the FD, this requiring an
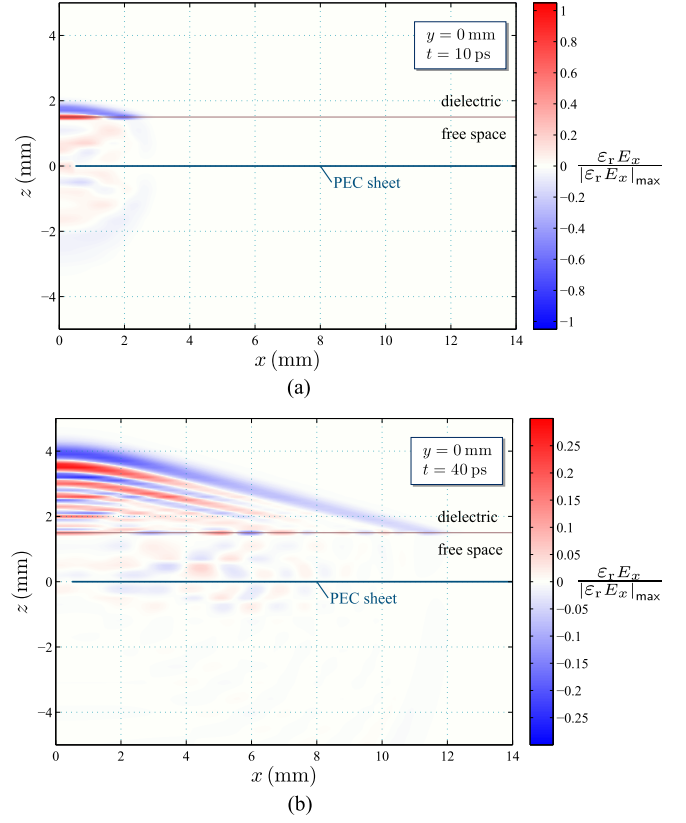

Fig. 15.   Aggregate field in the $x = 0$ plane, combining the effect of four pulses spaced at 20 ps. The gap height is (a) $h = 0.5$ mm and (b) $h = 1$ mm. $|\varepsilon_\mathrm{r} E_x|_{\max}$ is the maximum of $|\varepsilon_\mathrm{r} E_x|$ over all snapshots.

established steady-state TH operation. However, the current trend toward higher data rates and increasingly sophisticated modulations constantly compress the interval of validity of the steady-state, TH assumption. The results of this article allow
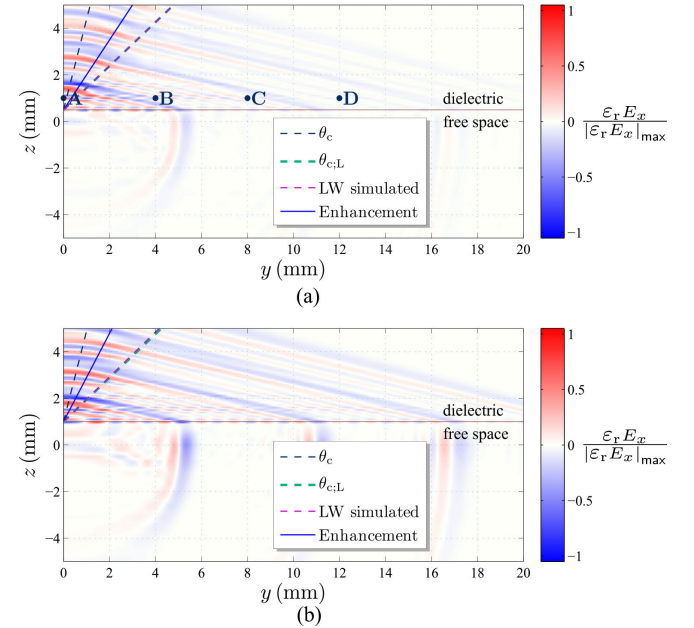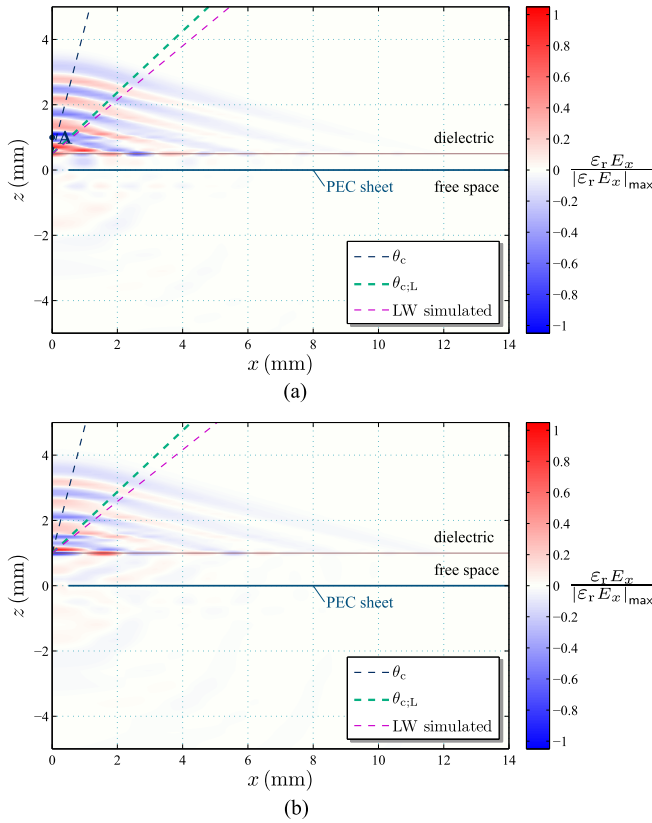
Fig. 16.   Aggregate field in the $y = 0$ plane, combining the effect of four pulses spaced at $10\,\mathrm{ps}$. The gap height is (a) $h = 0.5\,\mathrm{mm}$ and (b) $h = 1\,\mathrm{mm}$. $|\varepsilon_{\mathrm{r}} E_x|_{\mathsf{max}}$ is the maximum of $|\varepsilon_{\mathrm{r}} E_x|$ over all snapshots. Point A in Fig. 1 is shown in (a) for reference.

understanding the transient EM effects after the steady-state was interrupted and *predicting* the behavior of the LW antennas during the transition to a new steady state.

The performed fully numerical analysis can intrinsically yield *total fields*, only. At this point, it is observed that FD analysis may allow distinguishing between different field constituents, as demonstrated in [11], [12], [25], [26], and [27]. In the realm of TD formulations, the Cagniard–de Hoop technique [28] provides the analytic instruments for distinguishing between HWs and BWs. Although these constituents never occur simultaneously for the same ray, the conjunction of all rays propagating within a finite time window offers structural information on the radiated field at any location and instant. By separating the EM field into constituents (either via FD instruments or via ray decomposition), it becomes possible to optimize separately the features of the radiating structures that, in turn, yields additional design degrees of freedom. Alternatively, the total field estimation is equally relevant— for example, the total field at given reference planes can be further propagated through overlay structures, as habitually done in the design of lens antennas. Whichever of the two paths (component decomposition versus total field calculation) is more effective depends, eventually, on the design problem.

To conclude with, a purely computational observation must also be made. During constructing the field snapshots, it was noticed that significant field values were recorded in the FIT data beyond the limit where the EM wave should arrive at the snapshots' timing. While finite-difference, TD (and, implicitly, FIT) solutions can be, potentially, affected by supraluminal artifacts caused by grid dispersion [29], [30], [31], such effects are extremely unlikely in the present experiments due to the employed mesh density. Consequently, the observed spurious values may originate from either one of the following: 1) the cell size (0.5 mm in the y-direction along the slot) in combination with the interpolation at intermediate locations; 2) small deviations in the selection of the frame for which the FIT code generates the plot data; and 3) specific choices in the FIT marching-on-in-time implementation. The entailed inconsistencies translate into the actual timing of the retrieved datasets being affected by some degree of uncertainty, definitely at the sub-ps-level demanded by this study. These inconsistencies have a twofold negative effect: 1) They may lead to visible discrepancies between theoretically predicted and observed features in zoomed-in plots; to circumvent suchlike discrepancies, the theoretical wavefronts were consistently aligned to the simulated ones and 2) they may result in jitter-type errors when combining data for assembling the response to pulse trains. This type of error was deemed acceptable for the (preliminary) studies reported in this article, but can become a matter of concern when an extremely accurate combination of sequences is aimed at. Methods for improving the accuracy of the timing of the retrieved datasets are under investigation.

VI. Conclusion

Weakly dispersive, LW configurations encountered in LW antennas were subject to a causal, TD, numerical investigation. First, some important analytical results were conclusively validated by examining the radiation from a gap-fed slot in a PEC sheet at a plane dielectric–free-space interface. The first result was demonstrating the EM field enhancement along a direction that coincided with the structure's LW critical angle calculated in [16]. In a second phase, a similar configuration, with the dielectric being slightly elevated above the PEC, was examined in view of generating insight in the TD operation of LLAs. In this respect, typical FD features of the radiated EM field could be recognized in *pulsed-field* snapshots. The experiments revealed a field partition into a laminar, conical-wave-type zone at the wave's forefront and a spherical-waves-type zone above the feeding gap, separated via a narrow, abrupt transition. Remarkably, the limit of the conical-wave-type zone was, practically, at the LW critical angle. Moreover, a clear field enhancement was evidenced in the transition zone, the direction along which this enhancement manifested itself coming closer to the normal to the interface for increasing dielectric-to-PEC spacing. This behavior could be put in correspondence with the so-called shadow boundary inferred via FD instruments, thus giving additional, this time, TD arguments for the crucial role of the air gap in the operation of LLAs. To conclude with, studying the response to trains of equally spaced pulses laid the first steps toward building a conceptual bridge between the TD and FD models of the LW radiation.

ACKNOWLEDGMENT

REFERENCES

[1] Z. Chen et al., "Terahertz wireless communications for 2030 and beyond: A cutting-edge frontier," *IEEE Commun. Mag.*, vol. 59, no. 11, pp. 66–72, Nov. 2021.

[2] A. Neto, "UWB, non dispersive radiation from the planarly fed leaky lens antenna—Part 1: Theory and design," *IEEE Trans. Antennas Propag.*, vol. 58, no. 7, pp. 2238–2247, Jul. 2010.

[3] N. Llombart, G. Chattopadhyay, A. Skalare, and I. Mehdi, "Novel terahertz antenna based on a silicon lens fed by a leaky wave enhanced waveguide," *IEEE Trans. Antennas Propag.*, vol. 59, no. 6, pp. 2160–2168, Jun. 2011.

[4] N. T. Nguyen, R. Sauleau, and L. Le Coq, "Reduced-size double-shell lens antenna with flat-top radiation pattern for indoor communications at millimeter waves," *IEEE Trans. Antennas Propag.*, vol. 59, no. 6, pp. 2424–2429, Jun. 2011.

[5] I. Vakili, L. Ohlsson, M. Gustafsson, and L. E. Wernersson, "Wideband and non-dispersive wavelet transmission using leaky lens antenna," *Electron. Lett.*, vol. 49, no. 5, pp. 321–322, Feb. 2013, doi: 10.1049/el.2013.0005.

[6] A. Neto, N. Llombart, J. J. A. Baselmans, A. Baryshev, and S. J. C. Yates, "Demonstration of the leaky lens antenna at submillimeter wavelengths," *IEEE Trans. Terahertz Sci. Technol.*, vol. 4, no. 1, pp. 26–32, Jan. 2014.

[7] L. Ohlsson, D. Sjöberg, and L.-E. Wernersson, "Codesign of compact III–V millimeter-wave wavelet transmitters with on-chip antennas," *IEEE Trans. Microw. Theory Techn.*, vol. 66, no. 1, pp. 273–279, Jan. 2018.

[8] S. van Berkel et al., "Wideband double leaky slot lens antennas in CMOS technology at submillimeter wavelengths," *IEEE Trans. Terahertz Sci. Technol.*, vol. 10, no. 5, pp. 540–553, Sep. 2020.

[9] A. Neto and S. Maci, "Green's function for an infinite slot printed between two homogeneous dielectrics. I. Magnetic currents," *IEEE Trans. Antennas Propag.*, vol. 51, no. 7, pp. 1572–1581, Jul. 2003.

[10] S. Maci and A. Neto, "Green's function of an infinite slot printed between two homogeneous dieletrics—Part II: Uniform asymptotic solution," *IEEE Trans. Antennas Propag.*, vol. 52, no. 3, pp. 666–676, Mar. 2004.

[11] F. Mesa, D. R. Jackson, and M. J. Freire, "High-frequency leaky-mode excitation on a microstrip line," *IEEE Trans. Microw. Theory Techn.*, vol. 49, no. 12, pp. 2206–2215, Dec. 2001.

[12] R. Rodriguez-Berral, F. Mesa, and D. R. Jackson, "A high-frequency circuit model for the gap excitation of a microstrip line," *IEEE Trans. Microw. Theory Techn.*, vol. 54, no. 12, pp. 4100–4110, Dec. 2006.

[13] F. Frezza, P. Lampariello, R. Moretti, P. Nocito, and M. Tsuji, "Application of FDTD method to the analysis and design of leaky-wave antennas at microwaves and millimeter waves," *Int. J. Infr. Millim. Waves*, vol. 29, no. 5, pp. 457–464, Mar. 2008, doi: 10.1007/s10762-008-9342-0.

[14] M. M. Azari, S. Solanki, S. Chatzinotas, and M. Bennis, "THz-empowered UAVs in 6G: Opportunities, challenges, and trade-offs," *IEEE Commun. Mag.*, vol. 60, no. 5, pp. 24–30, May 2022.

[15] D. Kralj and L. Carin, "Time-domain characteristics of slotted-waveguide leaky-wave antennas," *IEEE Microw. Guided Wave Lett.*, vol. 7, no. 5, pp. 124–126, May 1997.

[16] M. Stumpf, J. Gu, and I. E. Lager, "Time-domain electromagnetic leaky waves," *IEEE Trans. Antennas Propag.*, vol. 71, no. 4, pp. 3382–3392, Apr. 2023.

[17] J. Gu, A. Neto, I. E. Lager, and M. Stumpf, "Wave-front behaviour of the pulsed EM field—Complexity and implications," in *Proc. 17th Eur. Conf. Antennas Propag. (EuCAP)*, Mar. 2023, pp. 1–5.

[18] J. Gu, M. Štumpf, A. Neto, and I. E. Lager, "Pulsed operation of a weakly-dispersive, leaky-wave antenna: A causal numerical study–supplementary material," to be published, doi: 10.1109/TAP.2023.3338006.

[19] F. Mesa, C. di Nallo, and D. R. Jackson, "The theory of surface-wave and space-wave leaky-mode excitation on microstrip lines," *IEEE Trans. Microw. Theory Techn.*, vol. 47, no. 2, pp. 207–215, Feb. 1999.

[20] D. R. Jackson et al., "The fundamental physics of directive beaming at microwave and optical frequencies and the role of leaky waves," *Proc. IEEE*, vol. 99, no. 10, pp. 1780–1805, Oct. 2011.

[21] W. C. Chew, *Waves and Fields in Inhomogeneous Media*, 2nd ed. Piscataway, NJ, USA: IEEE Press, 1995.

[22] F. Frezza and N. Tedeschi, "Electromagnetic inhomogeneous waves at planar boundaries: Tutorial," *J. Opt. Soc. Amer. A, Opt. Image Sci.*, vol. 32, no. 8, pp. 1485–1501, Aug. 2015, doi: 10.1364/josaa.32.001485.

[23] I. E. Lager and S. L. van Berkel, "Finite temporal support pulses for EM excitation," *IEEE Antennas Wireless Propag. Lett.*, vol. 16, pp. 1659–1662, 2017.

[24] I. E. Lager and A. T. de Hoop, "Time-domain receiving properties of a multimode cylindrical waveguide antenna," in *Proc. 5th Eur. Conf. Antennas Propag.*, 2011, pp. 1420–1423.

[25] F. Capolino, D. R. Jackson, and D. R. Wilton, "Fundamental properties of the field at the interface between air and a periodic artificial material excited by a line source," *IEEE Trans. Antennas Propag.*, vol. 53, no. 1, pp. 91–99, Jan. 2005.

[26] J. Bernal, F. Mesa, and D. R. Jackson, "Effects of losses on the current spectrum of a printed-circuit line," *IEEE Trans. Microw. Theory Techn.*, vol. 55, no. 7, pp. 1511–1519, Jul. 2007.

[27] W. Fuscaldo, "Rigorous evaluation of losses in uniform leaky-wave antennas," *IEEE Trans. Antennas Propag.*, vol. 68, no. 2, pp. 643–655, Feb. 2020.

[28] A. T. D. Hoop, "Pulsed electromagnetic radiation from a line source in a two-media configuration," *Radio Sci.*, vol. 14, no. 2, pp. 253–268, Mar. 1979, doi: 10.1029/RS014i002p00253.

[29] J. B. Schneider and C. L. Wagner, "FDTD dispersion revisited: Faster-than-light propagation," *IEEE Microw. Guided Wave Lett.*, vol. 9, no. 2, pp. 54–56, Feb. 1999.

[30] K. L. Shlager and J. B. Schneider, "Comparison of the dispersion properties of several low-dispersion finite-difference time-domain algorithms," *IEEE Trans. Antennas Propag.*, vol. 51, no. 3, pp. 642–653, Mar. 2003.

[31] A. Taflove, S. C. Hagness, and M. Piket-May, "Computational electromagnetics: The finite-difference time-domain method," in *The Electrical Engineering Handbook*, W.-K. Chen, Ed. Amsterdam, The Netherlands: Elsevier, 2004, pp. 629–670.

Junhong Gu (Student Member, IEEE) was born in Weihai, Shandong, China, in December 3, 1997. He received the B.Sc. degree in electrical and electronic engineering from the University of Liverpool, Liverpool, U.K., in 2020, and the M.Sc. degree from the Terahertz Sensing Group, Delft University of Technology (TU Delft), Delft, The Netherlands, in 2022.

His research interests include applied electromagnetics, time-domain analysis of electromagetic wave phenomena, and the design of radio frequency power amplifier circuit and traveling-wave parametric amplifier circuit.

Martin Štumpf (Senior Member, IEEE) received the Ph.D. degree in electrical engineering from the Brno University of Technology (BUT), Brno, Czech Republic, in 2011.

He spent a year and a half as a Post-Doctoral Fellow with KU Leuven, Leuven, Belgium. During a three-month period in 2018, he was a Visiting Professor with the UAq EMC Laboratory, University of L'Aquila, L'Aquila, Italy. He is currently an Associate Professor of theoretical electrical engineering with the Lerch Laboratory of EM Research, BUT, and a Researcher with the EISLAB, University of Technology, Luleå, Sweden. He has authored the books *Electromagnetic Reciprocity in Antenna Theory* (Wiley–IEEE Press, 2017), *Pulsed EM Field Computation in Planar Circuits: The Contour Integral Method* (CRC Press, 2018), *Time-Domain Electromagnetic Reciprocity in Antenna Modeling* (Wiley–IEEE Press, 2019), and *Metasurface Electromagnetics: The Cagniard-DeHoop Time-Domain Approach* (IET, 2022). His main research interests include analytical and computational modeling of electromagnetic wave and diffusive phenomena with an emphasis on antenna theory and EMC.

Andrea Neto (Fellow, IEEE) received the Laurea degree (summa cum laude) in electronic engineering from the University of Florence, Florence, Italy, in 1994, and the Ph.D. degree in electromagnetics from the University of Siena, Siena, Italy, in 2000.

Part of his Ph.D. degree was developed at the European Space Agency Research and Technology Center, Noordwijk, The Netherlands. He worked at the Antenna Section, European Space Agency Research and Technology Center, for over two years. From 2000 to 2001, he was a Post-Doctoral Researcher with the California Institute of Technology, Pasadena, CA, USA, where he worked at the Submillimeter Wave Advanced Technology Group. From 2002 to January 2010, he was a Senior Antenna Scientist with TNO Defense, Security, and Safety, The Hague, The Netherlands. In February 2010, he became a Full Professor of applied electromagnetism at the Department of Electrical Engineering, Mathematics and Computer Science, Delft University of Technology, Delft, The Netherlands, where he formed and leads the THz Sensing Group. His research interests include the analysis and design of antennas with an emphasis on arrays, dielectric lens antennas, wideband antennas, EBG structures, and THz antennas.

Dr. Neto is a member of the Technical Board of the European School of Antennas and an organizer of the course on antenna imaging techniques. He is also a member of the Steering Committee of the Network of Excellence NEW-FOCUS, dedicated to focusing techniques in millimeter and submillimeter-wave regimes. He was a recipient of the European Research Council Starting Grant to perform research on advanced antenna architectures for THz sensing systems in 2011, the H. A. Wheeler Award for the Best Applications Paper of 2008 in IEEE TRANSACTIONS ON ANTENNAS AND PROPAGATION, the Best Innovative Paper Prize of the 30th ESA Antenna Workshop in 2008, and the Best Antenna Theory Paper Prize of the European Conference on Antennas and Propagation (EuCAP) in 2010. He served as an Associate Editor for IEEE TRANSACTIONS ON ANTENNAS AND PROPAGATION from 2008 to 2013 and IEEE ANTENNAS AND WIRELESS PROPAGATION LETTERS from 2005 to 2013.

Ioan E. Lager (Senior Member, IEEE) received the Ph.D. degrees in electrical engineering from the Delft University of Technology, Delft, The Netherlands, in 1996, and the Transilvania University of Braşov, Braşov, Romania, in 1998.

In 1997, he was a Visiting Scientist with Schlumberger-Doll Research, Ridgefield, CT, USA. He successively occupied research and academic positions with the Transilvania University of Braşov and the Delft University of Technology, where he is currently an Associate Professor. He endeavors toward bridging the gap between electromagnetic field theory and the design, implementation, and measurement of antenna front-end architectures. His research interests include applied electromagnetics, especially time-domain propagation and applications, and antenna engineering, with an emphasis on nonperiodic (interleaved) array antenna architectures.